Supplemental Materials

A minimal model of an artificial topological material realized in a two-terminal Josephson junction threaded by Aharonov-Casher fluxes

Luka Medic,[*] Anton Ramšak, and Tomaž Rejec
Jožef Stefan Institute, Jamova 39, SI-1000 Ljubljana, Slovenia and
Faculty of Mathematics and Physics, University of Ljubljana, Jadranska 19, SI-1000 Ljubljana, Slovenia
(Dated: November 18, 2025)

S1. BOGOLIUBOV-DE GENNES HAMILTONIAN OF THE MODEL

Here, we provide the Bogoliubov-de Gennes (BdG) Hamiltonian of the system in a block matrix form

$$\mathcal{H}_{\mathrm{BdG}} = \begin{bmatrix} \mathcal{H}_l & \mathcal{H}_{T,l}^\dagger & 0 \\ \mathcal{H}_{T,l} & \mathcal{H}_{QD} & \mathcal{H}_{T,r} \\ 0 & \mathcal{H}_{T,r}^\dagger & \mathcal{H}_r \end{bmatrix}, \tag{1}$$

where the subsystems are defined as follows. The BdG Hamiltonians describing the left ($\mathcal{H}_l$) and right ($\mathcal{H}_r$) superconducting leads take the form

$$\mathcal{H}_{l/r} = \begin{bmatrix} h_{l/r} & \Delta_{l/r} \\ \Delta_{l/r}^* & -h_{l/r} \end{bmatrix}. \tag{2}$$

The normal-state Hamiltonians for the semi-infinite left and right leads are

$$h_l = \begin{bmatrix} \ddots & \ddots & & \\ \ddots & \ddots & -\gamma & \\ & -\gamma & 0 & -\gamma \\ & & -\gamma & 0 \end{bmatrix} \otimes \sigma_0, \quad h_r = \begin{bmatrix} 0 & -\gamma & & \\ -\gamma & 0 & -\gamma & \\ & -\gamma & \ddots & \ddots \\ & & \ddots & \ddots \end{bmatrix} \otimes \sigma_0, \tag{3}$$

where σ_0 is the 2×2 identity matrix acting on the spin degree of freedom. The superconducting pairing is described by

$$\Delta_l = e^{i\phi} \begin{bmatrix} \ddots & & & \\ & \ddots & & \\ & & \Delta & \\ & & & \Delta \end{bmatrix} \otimes \sigma_0, \quad \Delta_r = \begin{bmatrix} \Delta & & & \\ & \Delta & & \\ & & \ddots & \\ & & & \ddots \end{bmatrix} \otimes \sigma_0. \tag{4}$$

The central region, consisting of two interconnected quantum dots (QDs), is described by

$$\mathcal{H}_{QD} = \begin{bmatrix} H_{QD} & 0 \\ 0 & -H_{QD} \end{bmatrix}, \qquad H_{QD} = \begin{bmatrix} u' & -\gamma' \\ -\gamma' & u' \end{bmatrix} \otimes \sigma_0. \tag{5}$$

Finally, the matrices describing the tunneling between the superconducting leads and the QDs are

$$\mathcal{H}_{T,l/r} = \begin{bmatrix} H_{T,l/r} & 0 \\ 0 & -H_{T,l/r} \end{bmatrix}, \tag{6}$$

where

$$H_{T,l} = -\gamma' \begin{bmatrix} \cdots & 0 & 0 & \sigma_0 \\ \cdots & 0 & 0 & e^{i\alpha_1 \sigma_z} \end{bmatrix}, \quad H_{T,r} = -\gamma' \begin{bmatrix} \sigma_0 & 0 & 0 & \cdots \\ e^{-i\alpha_2 \sigma_z} & 0 & 0 & \cdots \end{bmatrix}. \tag{7}$$

Here, σ_z is the Pauli matrix acting on the spin degree of freedom.

---

[*] l.medic@windowslive.com

S2. ANALYTICAL TREATMENT OF THE MODEL

The closed-form expressions for the reflection and transmission amplitudes for an electron with spin ↑ incoming from the left lead are

$$r(\alpha_1,\alpha_2) = \left(-1+\frac{2\gamma^2\left((u')^2-(\gamma')^2\right)-4i\gamma(\gamma')^2\left(u'+\gamma'\cos(\alpha_2)\right)}{\gamma^2\left((u')^2-(\gamma')^2\right)+2(\gamma')^4\left(1-\cos(\alpha_1+\alpha_2)\right)+2i\gamma(\gamma')^3\left(\cos(\alpha_1)-\cos(\alpha_2)\right)}\right)^{-1}, \tag{8a}$$

$$t(\alpha_1,\alpha_2) = \frac{2i\gamma(\gamma')^2\left[u'\left(1+e^{i(\alpha_1+\alpha_2)}\right)+\gamma'\left(e^{i\alpha_1}+e^{i\alpha_2}\right)\right]}{\gamma^2\left((u')^2-(\gamma')^2\right)-4i\gamma(\gamma')^2u'-2(\gamma')^4\left(1-\cos(\alpha_1+\alpha_2)\right)-2i\gamma(\gamma')^3\left(\cos(\alpha_1)+\cos(\alpha_2)\right)}. \tag{8b}$$

Due to the left-right mirror symmetry of the model (see Fig. 1 of the main text), the reflection and transmission amplitudes for an incoming electron from the right lead are $r'(\alpha_1,\alpha_2) = r(-\alpha_2,-\alpha_1)$ and $t'(\alpha_1,\alpha_2) = t(-\alpha_2,-\alpha_1)$, respectively.

For a two-terminal junction, the energy dispersion is given by $E_\pm(\vec{x}) = \pm\sqrt{1-T(\alpha_1,\alpha_2)\sin^2(\phi/2)}$ [1], where $T(\alpha_1,\alpha_2) = |t(\alpha_1,\alpha_2)|^2 = 1-|r(\alpha_1,\alpha_2)|^2$. Therefore, ABS band touchings ($E_\pm = 0$) occur when $\phi = \pi$ and $r = 0$. Hence, we obtain the condition for the ABS band gap closure by setting the denominator in Eq. (8a) to zero. Separating the real and imaginary parts, this leads to the conclusion that the system is gapless for $0 \le \frac{\gamma^2\left((\gamma')^2-(u')^2\right)}{4(\gamma')^4} \le 1$ at $\alpha_W = \alpha_1 = \alpha_2 = \frac{1}{2}\arccos\left(1-\frac{\gamma^2\left((\gamma')^2-(u')^2\right)}{2(\gamma')^4}\right)$.

The system exhibits SC gap edge touchings if and only if $\phi = 0$ or $t = 0$. The condition $t = 0$ is satisfied by setting the numerator of Eq. (8b) to zero, leading to the following expression:

$$e^{i\alpha_2} = -\frac{u'+\gamma' e^{i\alpha_1}}{\gamma'+u'\,e^{i\alpha_1}}. \tag{9}$$

By satisfying this constraint separately for the real and imaginary parts, we obtain

$$\alpha_2 = \pm\arccos\left(-\frac{2u'\gamma'+\left((u')^2+(\gamma')^2\right)\cos(\alpha_1)}{(u')^2+(\gamma')^2+2u'\gamma'\cos(\alpha_1)}\right) \tag{10}$$

with $+$ and $-$ signs for $\alpha_1 \in [-\pi, 0)$ and $\alpha_1 \in [0,\pi)$, respectively. Thus, instead of having SC gap-edge-touching nodes, the system possesses a closed SC gap-edge-touching line, as depicted in Fig. 3(b) of the main text (dashed).

For the derivatives of the reflection amplitude r, evaluated at $\alpha_W = \alpha_1 = \alpha_2$, which indicates the position of the Weyl node at $\vec{x}_W = [\alpha_W, \alpha_W, \pi]^T$, we compute

$$\left.\frac{\partial r}{\partial \alpha_{1,2}}\right|_{\alpha_{1,2}=\alpha_W} = \frac{2(\gamma')^3\left(\gamma'\sin(2\alpha_W)\mp i\gamma\sin(\alpha_W)\right)}{2\gamma\left((u')^2-(\gamma')^2\right)-4i\gamma(\gamma')^2\left(u'+\gamma'\cos(\alpha_W)\right)} \tag{11}$$

where $-$ $(+)$ sign is taken for the derivative with respect to α_1 (α_2).

Based on our previous work [2], we know that the topological charge q_W can be computed as

$$q_W = \operatorname{sgn}\left[\det(M_2)\right] = \operatorname{sgn}\left[\operatorname{Im}\left(\frac{\partial\zeta}{\partial\alpha_1}\cdot\frac{\partial\zeta^*}{\partial\alpha_2}\right)\right]_{\vec{x}=\vec{x}_W}, \tag{12}$$

where

$$M_2 = \begin{bmatrix}\partial_{\alpha_1}\mathrm{Re}(\zeta) & -\partial_{\alpha_1}\mathrm{Im}(\zeta)\\ \partial_{\alpha_2}\mathrm{Re}(\zeta) & -\partial_{\alpha_2}\mathrm{Im}(\zeta)\end{bmatrix}_{\vec{x}=\vec{x}_W}, \qquad \zeta(\vec{x}) = \langle a_e^+|H(\vec{x})|a_e^-\rangle. \tag{13}$$

Here, H denotes the effective (electron) Hamiltonian within the ABS subspace [refer to Eq. (5) in the main text], and $|a_e^\pm\rangle$ represent the chiral states at the Weyl node with positive and negative chirality, respectively. For a 2×2 scattering matrix S, these states can be expressed as

$$|a_e^+\rangle = \begin{bmatrix}V_1(\vec{x}_W)\\ 0\end{bmatrix}, \qquad |a_e^-\rangle = \begin{bmatrix}0\\ V_2(\vec{x}_W)\end{bmatrix}. \tag{14}$$

where $V_1 = r/|r| \equiv e^{i\theta_r}$ and $V_2 = -i\,t/|t| \equiv -i\,e^{i\theta_t}$ are complex numbers derived from the polar decomposition of S [3, 4], which takes the form

$$S \equiv \begin{bmatrix} r & t'\\ t & r'\end{bmatrix} = \begin{bmatrix}V_1 & 0\\ 0 & V_2\end{bmatrix}\begin{bmatrix}-i|r| & |t|\\ |t| & -i|r|\end{bmatrix}\begin{bmatrix}U_1^\dagger & 0\\ 0 & U_2^\dagger\end{bmatrix}, \qquad U_1 = -i, \quad U_2 = r(t')^*/|rt| \equiv e^{i(\theta_r-\theta_{t'})}. \tag{15}$$

Note that from the unitarity of S, it follows $rt^* + t'(r')^* = 0$. Since $r(\vec{x}_W) = 0$, the derivatives in Eq. (12) reduce to

$$\frac{\partial \zeta}{\partial \alpha_i}(\vec{x}_W) = \Delta e^{-i\theta_r(\vec{x}_W)} \frac{\partial r}{\partial \alpha_i}(\vec{x}_W), \tag{16}$$

which further simplifies the expression for the topological charge to

$$q_W = \mathrm{sgn}\left[\mathrm{Im}\left(\frac{\partial r}{\partial \alpha_1} \cdot \frac{\partial r^*}{\partial \alpha_2}\right)\right]_{\alpha_{1,2}=\alpha_W}. \tag{17}$$

Using Eq. (11), we can show that this evaluates to

$$q_W = -\mathrm{sgn}\left[\sin(\alpha_W)\sin(2\alpha_W)\right] = -\mathrm{sgn}\left[\cos(\alpha_W)\right], \tag{18}$$

which demonstrates the validity of Eq. (4) in the main text.

S3. ANALYSIS OF PROTOCOL PARAMETERS

In the analysis of the protocol parameters, we vary the number of revolutions around the polar axis, N, and the duration of the driving protocol, τ_0. The results are presented in Fig. S1. Even for $N = 8$, the driving protocol sufficiently samples typical values of the Berry curvature, enabling the recovery of the topological charge q_W. On the other hand, the correspondence between $\mathcal{Q}$ and the enclosed topological charge q_W deteriorates when the assumption of adiabatic driving is not fulfilled for sufficiently short τ_0. Specifically, as shown in Fig. S1(b), this happens at $\tau_0 = 2 \cdot 10^4$ (in units of $\hbar/\Delta$). At this value, the time scale of one revolution around the polar axis, $\frac{\tau_0}{2N} \approx 300$, becomes comparable to the time scale associated with the energy gap $\tau_{\mathrm{gap}} = \frac{h}{\epsilon_{\mathrm{gap}}} \approx 30$. The two time scales, with faster and slower oscillations, can be explicitly seen in the results for currents presented in Fig. S2.

Additionally, in Fig. S1, we observe that as N decreases, the spikes at the edges of the quantized plateaus become less prominent or vanish entirely. This happens because lower values of N reduce the likelihood of closely approaching the Weyl nodes, thereby better preserving the adiabatic assumption. Furthermore, the asymmetry in the shape of $\mathcal{Q}$ around each Weyl node q_i becomes more pronounced. This increased asymmetry near the transitions results from the sparser path coverage of the sphere at smaller N.

S4. EXTENSION TO MULTI-CHANNEL LEADS

We extended our analysis to leads with multiple channels, specifically examining two coupled copies of the system described in the main text with inter-lead hopping, $\gamma_\perp$. In Fig. S3, we show results for (a) one copy, (b) two uncoupled copies, and (c) two coupled copies with $\gamma_\perp = 0.2\gamma$. In contrast to the main text, where r is a scalar, the top panels show $\arg(\det r)$ [2], since, in general, r is an $N_L \times N_L$ matrix, where N_L represents the number of channels in the left lead. Notably, in Fig. S3(b), the complex phase of $\det r$ is doubled. When the inter-lead coupling is nonzero [Fig. S3(c)], nodes with topological charge ±2 split into pairs of Weyl nodes with charges ±1.

The middle panels display the ABS dispersions at $\phi = \pi$ along the diagonal $\alpha = \alpha_1 = \alpha_2$, while the bottom panels present the results of the driving protocol with the sphere's center positioned along this diagonal. For two uncoupled copies, the currents double, resulting in the measurement of topological charges ±2. For $\gamma_\perp = 0.2\gamma$, the Weyl nodes $q_3^{(1,2)}$ are sufficiently far apart to be distinguishable by our protocol, whereas $q_4^{(1,2)}$ are separated by less than R in the (α_1, α_2) plane. With a sphere radius $R = 0.2$, both Weyl nodes can be enclosed simultaneously, leading to a plateau at $\mathcal{Q} = 2$ in Fig. S3(c). Nonetheless, the Weyl nodes remain distinguishable, as indicated by narrow plateaus at 1. The distinguishability of the nodes would improve in the adiabatic limit.

S5. FORMULATION OF TIME EVOLUTION IN THE NAMBU SPACE

In Ref. [2], we introduced an alternative approach to computing topological invariants that accounts for the entire Nambu space, treating both the electron and hole components of ABSs rather than focusing solely on

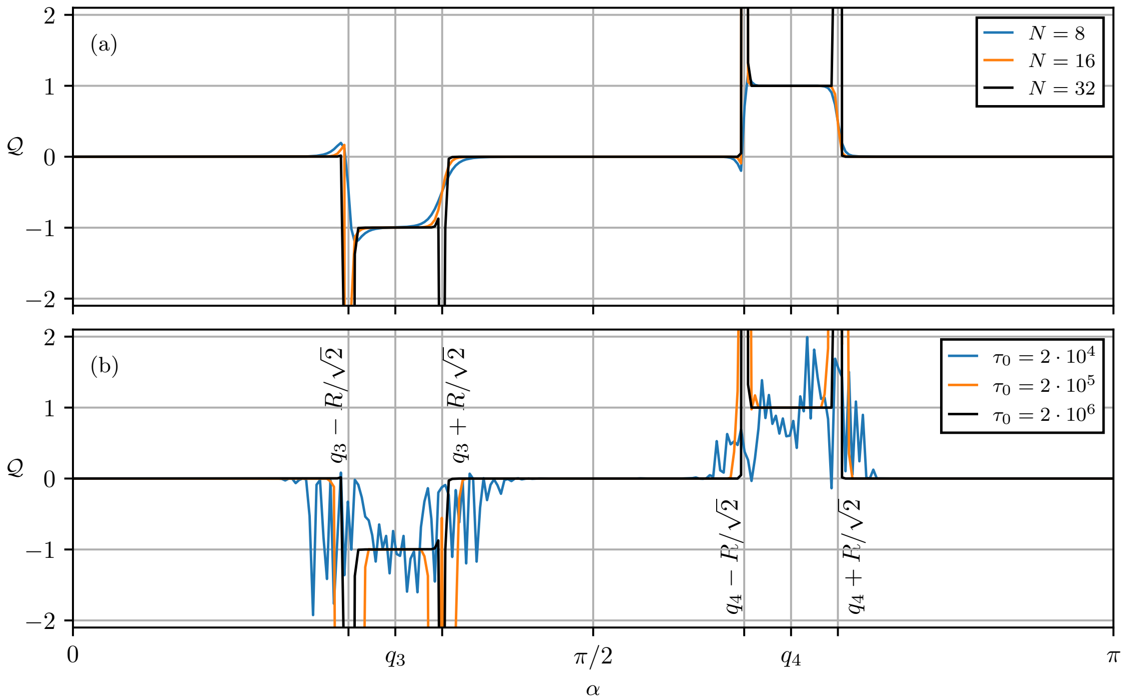

Figure S1. The path-averaged kinematic curvature $\mathcal{Q}$, with the center of the sphere at $\vec{x}_0 = [\alpha, \alpha, \pi]^T$. The parameters used are consistent with those in Fig. 5 of the main text. Panels (a) and (b) depict comparisons for distinct values of N and τ_0, respectively.

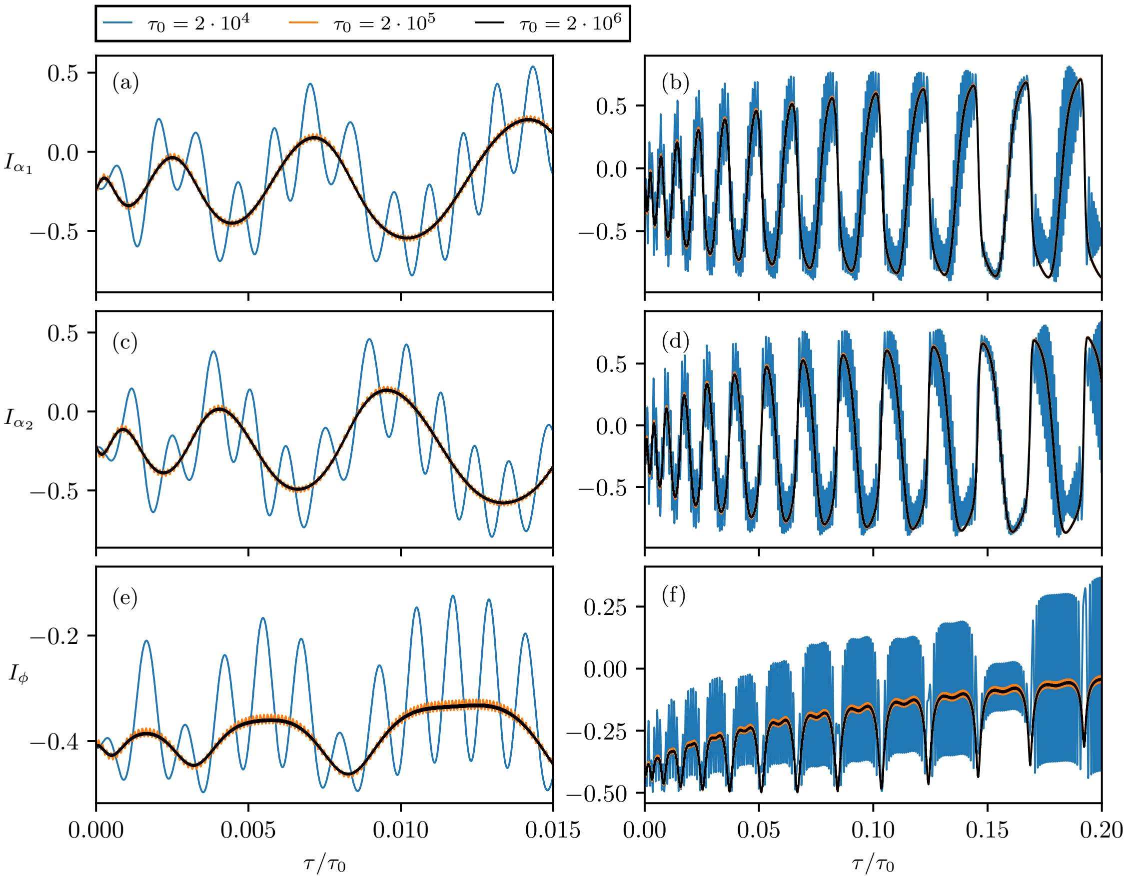

Figure S2. Currents for different driving periods τ_0. The left and right panels display shorter and longer time windows, respectively. For $\tau_0 = 2 \cdot 10^4$ (non-adiabatic regime), the two time scales, $\tau_{\text{gap}} \approx 30$ and $\tau_0/(2N) \approx 300$, are comparable.

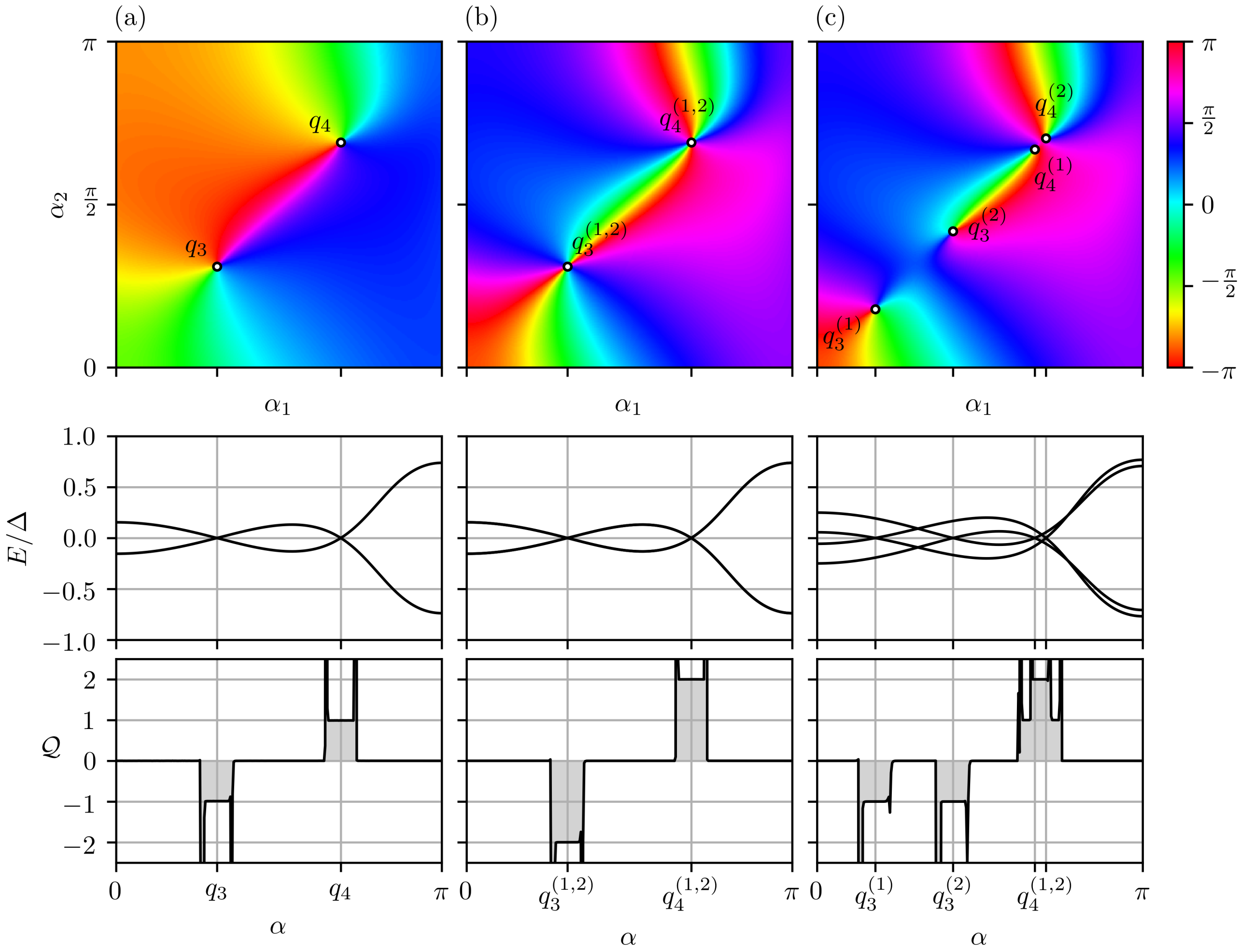

Figure S3. *Top panels*: phases of the determinant of the reflection matrix at the left lead, $\arg(\det r)$, plotted in the plane of AC fluxes α_1 and α_2, with the positions of the Weyl nodes labeled by q_i. *Middle panels*: energy dispersions of the ABSs as a function of $\alpha = \alpha_1 = \alpha_2$. *Bottom panels*: the path-averaged kinematic curvature $\mathcal{Q}$, illustrating its relationship to the Weyl node charges enclosed by a sphere centered at (α, α, π). Plateaus correspond to quantized topological charges of ± 1 or ± 2, depending on whether the Weyl nodes are resolved individually or enclosed together.

the electron part. Here, we extend this formalism to compute the time evolution of the wave function and the currents by utilizing the basis of instantaneous eigenfunctions and propagating the corresponding coefficients in time. Using these eigenfunctions as the basis is crucial, as the ABSs span only a submanifold of the full Nambu space.

We work in the instantaneous basis of the ABSs $|\varphi_n(\tau)\rangle$ of the time-dependent BdG Hamiltonian $H(\tau)$:

$$H(\tau)|\varphi_n(\tau)\rangle = E_n(\tau)|\varphi_n(\tau)\rangle. \tag{19}$$

Solving the time-dependent equation

$$i\hbar|\dot{\psi}(\tau)\rangle = H(\tau)|\psi(\tau)\rangle, \tag{20}$$

where $|\psi(\tau)\rangle = \sum_n a_n(\tau)|\varphi_n(\tau)\rangle$ is written in the basis of instantaneous eigenfunctions, we obtain the system of differential equations governing the time evolution of the coefficients a_n:

$$\dot{a}_m(\tau) = -iE_m(\tau)a_m(\tau) - \sum_n \langle\varphi_m(\tau)|\dot{\varphi}_n(\tau)\rangle a_n(\tau). \tag{21}$$

To compute the nonadiabatic couplings $\langle\varphi_m(\tau)|\dot{\varphi}_n(\tau)\rangle$, a smooth structure gauge for the instantaneous eigenstates is required. This is obtained using polar decomposition [2]. For the particular case under study, with only two ABSs ($m, n \in \{+, -\}$), the desired result is

$$\begin{bmatrix}\varphi_+ & \varphi_-\end{bmatrix} = \frac{1}{2}\begin{bmatrix}\varphi_\alpha & \varphi_\beta\end{bmatrix}\begin{bmatrix}e^{-i\phi/4} & 0 \\ 0 & e^{i\phi/4}\end{bmatrix}\begin{bmatrix}1 & 1 \\ 1 & -1\end{bmatrix}\begin{bmatrix}z/|z| & 0 \\ 0 & 1\end{bmatrix}\begin{bmatrix}1 & 1 \\ 1 & -1\end{bmatrix}. \tag{22}$$

Here, $z = |t|\cos(\phi/2) - i|r|$, and

$$[\varphi_\alpha \quad \varphi_\beta] = \frac{1}{\sqrt{2}} \begin{bmatrix} 0 & r/|r| \\ -it/|t| & 0 \\ -i & 0 \\ 0 & -r(t')^*/|rt'| \end{bmatrix} \tag{23}$$

where the scattering matrix elements r, r', t, and t' all change with the AC fluxes α_1 and α_2, which are time dependent. Expectation values for the currents are obtained from

$$\vec{I}(\tau) = \langle\psi(\tau)|\nabla_{\vec{x}} H(\tau)|\psi(\tau)\rangle = \sum_n |a_n|^2 \nabla_{\vec{x}} E_n - \sum_{n\neq m} a_m^* a_n (E_m - E_n)\langle\varphi_m|\nabla_{\vec{x}}|\varphi_n\rangle. \tag{24}$$

This approach yields results nearly identical to those in Fig. S1, with only minor numerical deviations, especially near the transition points.

S6. EXACT TIME EVOLUTION OF THE BDG HAMILTONIAN

The effective electron Hamiltonian approach presented in the main text, along with its extension to the full Nambu space in Sec. S5, introduces several approximations to the exact solution of our toy model. Namely, the Andreev approximation assumes that the SC band gap is small compared to the bandwidth ($\Delta \ll \gamma$), the energy dependence of the scattering matrix is neglected, and the contribution of continuum states to currents is disregarded.

To check that our conclusions do not rely on any of those approximations, we perform the exact time evolution of the BdG Hamiltonian for the toy model with a finite number of sites per SC lead. Starting with the ground state at $\tau = 0$, we evolve the state in time and compute $\mathcal{Q}$. The results for $\Delta = 0.2\gamma$ and $L = 50$ sites per SC lead are shown in Fig. S4(b). Results are converged with respect to L. Note that the quantized plateaus in $\mathcal{Q}$ are slightly shifted compared to those obtained using the effective Hamiltonian approach. This is due to the finite value of Δ: the Andreev approximation is not strictly satisfied, resulting in a displacement of the Weyl nodes from their expected positions [see Fig. S4(a)]. We performed the calculation both with and without accounting for continuum states. The outcomes are indistinguishable (results including continuum states are not shown), confirming that the quantization of $\mathcal{Q}$ is exclusively due to ABS.

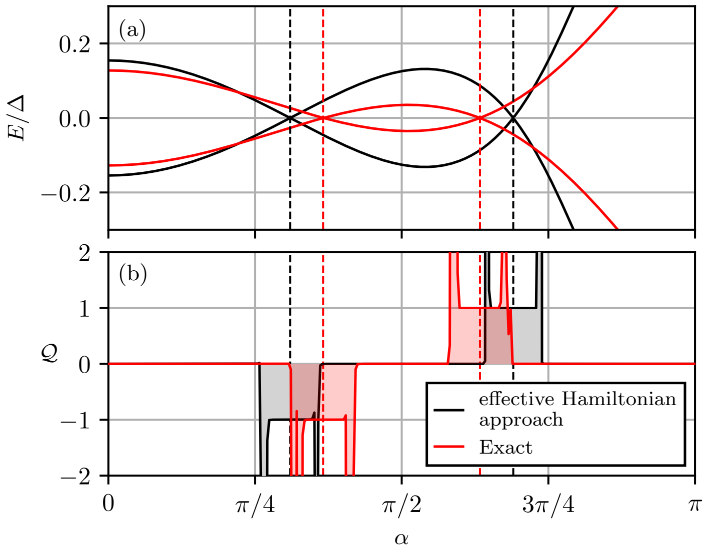

Figure S4. Comparison of the effective Hamiltonian approach presented in the main text with the exact solution: (a) energy dispersion and (b) quantization of $\mathcal{Q}$ as a function of α, with spheres centered at $[\alpha, \alpha, \pi]^T$. Dashed lines indicate the positions of the Weyl nodes.

[1] C. W. J. Beenakker, Universal limit of critical-current fluctuations in mesoscopic Josephson junctions, Phys. Rev. Lett. **67**, 3836 (1991).

[2] L. Medic, A. Ramšak, and T. Rejec, Artificial topological insulator realized in a two-terminal Josephson junction with Rashba spin-orbit interaction, Phys. Rev. Res. **7**, 013166 (2025).

[3] T. Martin and R. Landauer, Wave-packet approach to noise in multichannel mesoscopic systems, Phys. Rev. B **45**, 1742 (1992).

[4] C. W. J. Beenakker, Random-matrix theory of quantum transport, Rev. Mod. Phys. **69**, 731 (1997).